Journal of Materials Chemistry A

Accepted Manuscript

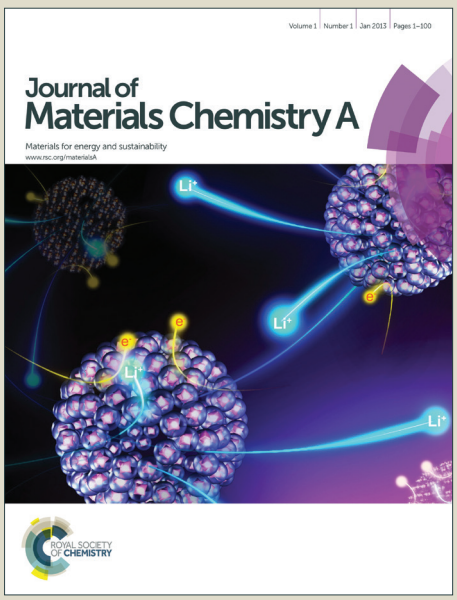

ROYAL SOCIETY OF CHEMISTRY

www.rsc.org/materialsA

Topotactical Conversion of Carbon Coated Fe-based Electrodes on Graphene Aerogels for Lithium Ion Storage

Feiying Jing and Yong Wang*

Department of Chemical Engineering, School of Environmental and Chemical Engineering, Shanghai University, Shangda Road 99, Shanghai, P. R. China, 200444

Email: yongwang@shu.edu.cn

Abstract: Iron oxides and iron sulfides have attracted significant research concerns for Lithium-ion batteries (LIBs) due to their larger theoretic capacity than the commercial electrode. However, they both suffer from large volume expansion during cycling and poor electrical conductivity. Iron sulfides have another problem of the dissolution of polysulfides into organic electrolyte. This work reports a sulfur-doped graphene aerogels (GAs) supported FeS_2@carbon composite with better lithium ion storage properties than its intermediate precursors (GAs supported Fe-Fe_3O_4@C and Fe_2O_3). It exhibits large reversible capacities of ~1000 mAh g^{-1} at 0.1 C during cycling with good rate capabilities. These enhanced electrochemical properties have been mainly attributed to the synergetic effect of GAs support, carbon coating and sulfur doping.

Keywords: graphene aerogels, carbon coating, sulfur doping, iron sulfide, iron oxide.

Introduction

Lithium-ion batteries (LIBs) are extensively used as the dominant power sources for portable electronic devices and electrical vehicles due to their high energy density and long cycle life.[1-5] Electrochemical performances of lithium ion batteries are closely related to their electrode materials. As a current commercial anode material, graphite has a limited theoretical capacity of 372 mAh g^{-1}. Recently, mental oxides (such as Fe_3O_4, Fe_2O_3, CuO, NiO) and metal sulfides (such as FeS_2, NiS, CoS, and SnS_2) have attracted significant research concerns due to the increasing demand for high capacity Li-storage.[6-17] In particular, Fe_3O_4 and FeS_2 both have high theoretic capacities of 928 mAh g^{-1} and 890 mAh g^{-1}, respectively.[8,14] Moreover, these Fe-based materials are also inexpensive, environmentally benign and naturally abundant.[6-8,11-14] However, these two materials both suffer from large volume expansion during cycling and the poor electrical conductivity. Iron disulfide (FeS_2) has another problem of the dissolution of polysulfides into an organic electrolyte.[18-20] All these problems have negative effect on their cycling performances for Li-ion storage.

Carbon support or coating is an effective approach to relieve the volume change and increase the electrical conductivity of high-capacity electrodes due to the soft and electrically-conductive nature of carbon.[1,2] Graphene has unique one-atom thick carbon structure and exhibits many intriguing properties when composited with other high-capacity materials. However few-layer graphene tends to restack to form thick

platelets and lose their unique properties.[21-24] Recently, three dimensional (3D) graphene aerogels (GAs) assembled from two dimensional graphene nanosheets have attracted significant research attention.[25-30] GAs usually exhibit improved macroporous structure and fast ion and electron transport kinetics due to their assembled 3D interconnected network structure. On the other hand, carbon coating is also a powerful strategy to increase the electrical conductivity of the coated materials. Hydrocarbon gas such as acetylene (C_2H_2) and methane (CH_4) have been reported as carbon sources to achieve uniform carbon coating in a chemical vapor deposition (CVD) process.[31-32] Furthermore, the modification of graphene with N, P, S, or B heteroatoms has been explored based on the theoretical calculation and experimental results. These heteroatoms can improve the electrical properties and electrochemical activities of graphene.[33-35]

In this work, the above three strategies were combined to obtain a carbon coated iron disulfides sphere on sulfur doped graphene aerogels (FeS_2@C/S-GAs). This hierarchical structure was prepared by a series of steps. The 3D interconnected composite structure (Fe_2O_3/GAs) was first prepared by a solvothermal method and then reacted with acetylene gas to obtain a carbon-coated structure on GAs (Fe-Fe_3O_4@C/GAs), which was finally converted to FeS_2@C/S-GAs in the presence of sulfur after a thermal treatment. These Fe-based electrodes were all explored with their Li-storage properties. It is found that the principal product of FeS_2@C/S-GAs exhibits the best electrochemical performances in terms of high capacity, good

cyclability and high-rate capability. It delivered a stable high capacity of ~1000 mAh g^{-1} during 80 cycles at 0.1C. When the current density increases from 0.1 C to 1 C, 2 C, 5 C, reversible capacities of 700 mAh g^{-1}, 630 mAh g^{-1}, 450 mAh g^{-1} could be still retained.

Experimental section

Material preparation

Graphene oxide (GO) was synthesized from natural graphite flake by a modified Hummers method, which was reported elsewhere.[36-37] Graphite nanopowders (XF NANO, 40 nm in thickness) was used to be exfoliated as the starting graphite.

Preparation of Fe_2O_3/GAs: 0.4 g $FeCl_3$•$6H_2O$ was dissolved into 10 ml deionized water to form a transparent yellow solution, which was then added dropwise into 40 ml of 1 mg ml^{-1} graphene oxide (GO) suspension. The mixture was heated at 80 ^oC for 5 h in a water bath. The resulting suspension was collected after centrifuging and copious washing with deionized water. The obtained materials were dispersed into 20 ml deionized water to form a brown suspension. The suspension was sealed in a 50 ml Teflon-lined stainless steel autoclave and then hydrothermally heated at 180 ^oC for 12 h. After cooling to room temperature, the black product was collected and freeze-dried overnight. As a control experiment, pristine Fe_2O_3 particles were prepared by a similar procedure in the absence of GO. Bare graphene aerogels (GAs) were also synthesized by hydrothermal heating and freeze-drying in the absence of $FeCl_3$.

Preparation of Fe-Fe_3O_4@C/GAs: The Fe_2O_3/GAs composite was put in a tube-like furnace and heated at 550 ^oC under flowing of pure N_2. The chemical vapor reduction and deposition reaction was performed at 550 ^oC by introducing a reactive gas mixture (5 % C_2H_2 and 95 % N_2, 35 sccm) for 10 min. The furnace was cooled slowly to room temperature in pure N_2.

Preparation of FeS_2@C/S-GAs: The obtained Fe-Fe_3O_4@C/GAs was mixed with elemental sulfur (w/w = 1:1) in a porcelain boat. A layer of aluminum foil was used to cover the boat and then heated in a tube furnace at 500 ^oC for 2 h in pure N_2. After the sulfuration reaction, the furnace was cooled gradually to room temperature in N_2. For comparison, pristine FeS_2 particles were synthesized in a similar process using the Fe_2O_3 particles as the starting reactant.

Materials characterizations

The as-prepared products were characterized by X-ray diffraction (XRD, Rigaku D/max-2550V, Cu Ka radiation), field-emission scanning electron microscopy (FE-SEM, JSM-6700F) with an energy dispersive X-ray spectrometer (EDS), and transmission electron microscopy (TEM, JEOL JEM-200CX). Raman spectroscopy was recorded on Renishaw in plus laser Raman spectrometer (excitation wavelength: 785 nm, excitation power: 3 mW, spot size: ~1.2 μm). The Brunauer-Emmett-Teller (BET) surface area and porous structures were tested by an accelerated surface area

and porosimetry analyzer (Micromeritics Instrument Corp, ASAP 2020 M + C, analysis adsorptive: N_2). The surface compositions of the products were evaluated by X-ray photoelectron spectra (XPS, PHI ESCA-5000C). Thermogravimetric analysis (TGA) was performed on a NETZSCH STA 409 PG/PC instrument in air atmosphere. Elemental analysis was performed on Vario MICRO.

Electrochemical measurements

The working electrodes were composed of 80 wt% of active material, 10 wt% of acetylene black (conductivity agent), and 10 wt% of polyvinylidene difluoride (PVDF) (binder). The loading amount of the electrode on copper foil was kept at ~2 mg cm^{-2} and the thickness of electrode materials was ~20 micrometers. The specific capacity was calculated based on the total weight of the active materials. Lithium foil was used as reference electrode. The electrolyte was $LiPF_6$ (1 M) dissolved in a 1:1 w/w mixture of ethylene carbonate (EC) and diethyl carbonate (DEC). The Swagelok-type cells were assembled in an argon-filled glove-box. Electrochemical measurements were performed on a LAND-CT2001C test system. The Swagelok-type cells were discharged (lithium insertion) and charged (lithium extraction) at different current densities (1 C = 890 mA g^{-1}) in the fixed voltage range of 5 mV to 3.0 V (*vs.* Li^+/Li). Cyclic voltammetry (CV) was performed on a CHI660D electrochemical workstation at a scan rate of 0.1 mV s^{-1}. Nyquist plots were collected on the same workstation for various electrodes from 100 kHz to 10 mHz.

Results and discussions

Materials synthesis and characterization

The stepwise synthetic process of three types of Fe-based electrodes (Fe_2O_3/GAs, Fe-Fe_3O_4@C/GAs, and FeS_2@C/S-GAs) is schematically illustrated in Scheme 1. First, Fe^{3+} ions from $FeCl_3$ may be attracted to the surface of GO sheets due to the existence of a large amount oxygen-containing groups (such as –OH). When the mixed solution is heated to 80 ^oC, the hydrolysis reaction is accelerated and Fe^{3+} ions are gradually changed to FeO(OH) on GO sheets.[38] Second, 2D GO sheets supported FeO(OH) can be self-assembled into a 3D porous graphene aerogels (GAs) network structure by a hydrothermal and freeze-drying treatment. In this process, GO is reduced to graphene and FeO(OH) is transformed into Fe_2O_3. Third, Fe_2O_3 is partly reduced to Fe and Fe_3O_4 by C_2H_2 gas due to a short reduction time (10 min). The obtained Fe is used as the *in situ* formed catalyst to decompose acetylene gas and promote the formation of carbon coating around Fe-Fe_3O_4 nanoclusters.[31,39] At last, the Fe and Fe_3O_4 are both reacted with elemental sulfur in N_2 atmosphere to form FeS_2. At this stage, some sulfur materials are found to be doped into GAs structure. Therefore the sulfur-doped GAs supported FeS_2@C is obtained as the final product. It is worthy noting that nanoparticle-assembled nanocluster structure can be retained for all three products (Fe_2O_3/GAs, Fe-Fe_3O_4@C/GAs, and FeS_2@C/GAs) and carbon coating structure can also be maintained for the latter two products in the stepwise preparation process with topotactical morphology conversion.

The XRD patterns of Fe_2O_3/GAs, Fe-Fe_3O_4@C/GAs and FeS_2@C/S-GAs are shown in Fig. 1a. The characteristic diffraction peaks of these samples can be respectively ascribed to the standard Fe_2O_3 (PDF 33-0664), Fe_3O_4 (PDF 65-3107) and FeS_2 (PDF 65-3321), except that the two extra diffraction peaks of Fe-Fe_3O_4@C/GAs at 25.8^o and 44.5^o are respectively assigned to GAs and Fe (PDF 65-4899). The peaks of GAs cannot be observed for Fe_2O_3/GAs and FeS_2@C/S-GAs, because the diffraction peaks of Fe_2O_3 and FeS_2 in these composites are so strong that they can shadow the diffraction peak of GAs.[8]

Fig. 1b shows TG analysis of the principal product of FeS_2@C/S-GAs and bare GAs in air. GAs can be gasified at a temperature range of ~400-500 ^{o}C. For the composite, two weight decreases (~380-500 ^{o}C and 600-700 ^{o}C) are ascribed to the gasification of carbon and the conversion of FeS_2 to Fe_2O_3. After high temperature treatment in air, the residual material is Fe_2O_3 (36.8 wt%).[12] Therefore, the weight percentage of FeS_2 in FeS_2@C/S-GAs can be estimated to be ~55.2 wt% (the sulfur content from FeS_2 is ~29.4 wt%). The FeS_2@C/S-GAs product was also characterized by elemental analysis, which is believed to be more accurate than TG. The weight contents of carbon and sulfur in this composite were determined to be ~26.5 wt% and 34.8 wt%, respectively. Therefore the weight content of the extra amount of sulfur may be estimated to be ~5.4 wt% in FeS_2@C/S-GAs. Fig. 1c shows the Raman spectra of GAs, Fe-Fe_3O_4@C/GAs and FeS_2@C/S-GAs. The D/G intensity ratios (I_D :

I_G) are 1.44, 1.45 and 1.53 respectively. The increase of the defects in FeS_2@C/S-GAs compared to Fe-Fe_3O_4@C/GAs is mainly attributed to the doped sulfur materials in GAs.[40] The BET measurements of GAs, Fe-Fe_3O_4@C/GAs and FeS_2@C/S-GAs were carried out to investigate specific surface area and pore size distribution. The N_2 adsorption-desorption isotherm of GAs is shown in Fig. 1d. GAs delivers a multi-point BET surface area (~45.1 m^2 g^{-1}) with dominated mesopores of ~11 nm (BJH analysis, the inset in Fig. 1d). In comparison, Fe-Fe_3O_4@C/GAs has a larger BET surface area of 99.4 m^2 g^{-1} (Fig. 1e) with mesopores of ~2.1 nm (the inset in Fig. 1e). Compared with Fe-Fe_3O_4@C/GAs, FeS_2@C/S-GAs has a smaller BET surface area of 24.5 m^2 g^{-1} as shown in Fig. 1f.

The digital photographs of the Fe_2O_3/GAs product before and after freeze-drying are respectively shown in Fig. 2a-b, which both present a macroscopical 3D structure. Its SEM images and TEM images are shown in Fig. 2c-d and Fig. 2e-f respectively. The GAs substrate reveals an interconnected 3D network architecture assembled by stacked graphene sheets with continuous pores of several micrometers. A large amount of Fe_2O_3 particles (~100-250 nm) are dispersed uniformly on both sides of graphene nanosheets. As a benchmarked sample, bare GAs with a macroporous structure is shown in SEM and TEM images of Fig. S1, Supporting Information. The XRD patterns of GAs, GNS and GO are all shown in Fig. S2，Supporting Information.

Fig. 3a-b show SEM images of Fe-Fe_3O_4@C/GAs. Compared with Fe_2O_3/GAs, the

3D macroporous structure can be retained for Fe-Fe_3O_4@C/GAs. A large number of particles (~150-320 nm in size) are immobilized on GAs. TEM images of the intermediate product of Fe-Fe_3O_4@C/GAs are shown in Fig. 3c-d. The supported Fe-Fe_3O_4@C nanoclusters are composed of a carbon overlayer (~10-15 nm in thickness) and a core consisting of many small Fe/Fe_3O_4 nanoparticles. The void pore space between carbon overlayer and nanoparticles can also be clearly seen as indicated by Fig. 3d.

Fig. 4a-c show SEM images of the principal final product of FeS_2@C/S-GAs. Compared with its precursor of Fe-Fe_3O_4@C/GAs, the morphology is largely retained. The EDS spectra of FeS_2@C/S-GAs is shown in Fig. 4d, which reveals the presence of C, O, Fe and S elements in the composite, in a good agreement with XPS and TGA results. A close observation of FeS_2@C structure is presented in TEM images of FeS_2@C/S-GAs (Fig. 4e-f). The product is still a core-shell structure and the carbon overlayer is indicated to be ~13 nm in thickness by Fig. 4f and the inset image showing the enlarged selected area. In comparison, pristine Fe_2O_3 and FeS_2 were also prepared. The XRD patterns of two control samples are shown in Fig. S3, Supporting Information, which reveals that all of diffraction peaks are corresponded to the standard Fe_2O_3 (PDF 33-0664) and FeS_2 (PDF 65-3321), respectively. SEM images of pristine Fe_2O_3 and FeS_2 particles are presented in Fig. S4, Supporting Information.

XPS measurements were carried out to analyze the surface composition of FeS_2@C/S-GAs. Fig. 5a is the XPS survey spectrum of the as-prepared product. There are five main peaks centered about 707.5 eV, 284.5 eV, 532.0 eV, 230.0 eV, and 164.0 eV, which can be corresponded to Fe 2p, C 1s, O 1s, S 2s and S 2p respectively. Fig. 5b shows the spectrum of C 1s, which consists of O-C=O (289.2 eV), C=O (288.0 eV), C-S (286.5 eV), C-C (285.7 eV) and C=C (284.5 eV) peaks.[41] Two strong peaks at ~707.5 eV and 720.2 eV are detected in the high-resolution XPS spectrum of Fe 2p in Fig. 5c, which can be assigned to the Fe $2p_{3/2}$ and Fe $2p_{1/2}$ from FeS_2.[42] The spectrum of S 2p is shown in Fig. 5d, which is composed of two main peaks. The peak located at ~169.0 eV is possibly attributed to the SO_4^{2-} on the surface of the FeS_2 particles.[42,43] Another peak located at ~164.0 eV can be divided into four characteristic peaks, which are located at ~165.2 eV (S $2p_{1/2}$ of the doped sulfur), 163.8 eV (S $2p_{3/2}$ of the doped sulfur and S $2p_{1/2}$ of FeS_2), 163.5 eV (the elemental sulfur) and 162.8 eV (S $2p_{3/2}$ of FeS_2).[42-44] The presence of a small amount of the doped sulfur and elemental sulfur is confirmed in the composite. Based on the quantitative results of XPS and previous elemental analysis, the doped sulfur and the elemental sulfur filled in the pores of GAs or carbon overlayer are estimated to be ~3.8 wt% and ~1.6 wt%, respectively.

Electrochemical performance

Fig. 6a shows the cyclic voltammograms of pristine FeS_2 at a scan rate of 0.1 mV s^{-1} between 3.0 V and 5 mV (*vs.* Li/Li^+), which can be used to investigate the reaction

mechanism between Li^+ and the electrode materials during cycling. In the first anodic scan, one reduction peak at ~1.15 V is observed. This single peak has been ascribed to the following two reduction reactions, which occur simultaneously in the first lithiation cycle.[13]

$$FeS_2 + 2Li^+ + 2e^- \rightarrow Li_2FeS_2$$

$$Li_2FeS_2 + 2Li^+ + 2e^- \rightarrow 2Li_2S + Fe^0$$

There are two peaks (~1.94 and 2.55 V) in the first cathodic scan, which correspond to the following two stepwise oxidation reactions:

$$Fe^0 + 2Li_2S \rightarrow Li_2FeS_2 + 2Li^+ + 2e^-$$

$$Li_2FeS_2 \rightarrow Li_{2-x}FeS_2 + xLi^+ + xe^- \ (0 < x < 0.8)$$

In the subsequent reduction-oxidation cycles, two reduction peaks (~1.82 V and 1.30 V) and two oxidation peaks (~1.98 V and 2.50 V) are observed, corresponding to the following two reversible reactions[13,19,45]:

$$Li_{2-x}FeS_2 + xLi^+ + xe^- \rightleftharpoons Li_2FeS_2 \ (0 < x < 0.8)$$

$$Li_2FeS_2 + 2Li^+ + 2e^- \rightleftharpoons Fe^0 + 2Li_2S$$

Fig. 6b presents the cyclic voltammograms of FeS_2@C/S-GAs at a scan rate of 0.1 mV s^{-1} between 3.0 V and 5 mV (*vs.* Li/Li^+). Compared with FeS_2, FeS_2@C/S-GAs exhibits similar peaks related to lithium reactions with FeS_2. There is an extra broad peak (~0.64 V) in the first anodic scan, which disappears in the second cycle. This should be ascribed to the electrolyte decomposition and the formation of solid electrolyte interface (SEI film) on the GAs electrode. The XRD patterns of the FeS_2@C/S-GAs electrode, discharged at ~1.3 V after 80 cycles, are shown in Fig.

S5, Supporting Information. There are diffraction peaks of GAs, Li_2S, Li_2FeS_2 and Fe. These results also confirm the lithium storage mechanism suggested above.

Fig. 6c presents the first-cycle discharge (lithium insertion) and charge (lithium extraction) of FeS_2@C/S-GAs and FeS_2 at 0.1 C, which exhibit initial discharge capacities of 1297.4, 1268.5 mAh g^{-1} and charge capacities of 923.4, 853.4 mAh g^{-1}, respectively. The first-cycle discharge and charge profiles of the other electrodes (GAs, Fe_2O_3/GAs, Fe_2O_3, Fe-Fe_3O_4@C/GAs) are shown in Fig. S6, Supporting Information. Initial discharge capacities of 1567.1, 1723.9, 1216.9, 995.9 mAh g^{-1} and charge capacities of 664.1, 1082.0, 822.1, 627.4 mAh g^{-1} are observed for these samples, respectively. Fig. 6d shows the cycling performances of the GAs, Fe_2O_3/GAs, Fe_2O_3 and Fe-Fe_3O_4@C/GAs electrodes at 0.1 C. There is a detectable capacity fading for bare GAs or pristine Fe_2O_3 electrode, which exhibits a low reversible capacity of 388.2 and 122.7 mAh g^{-1} respectively after 80 cycles. In the presence of GAs, the cycling performances of Fe_2O_3/GAs are stable (~1020 mAh g^{-1}) in the first 15 cycles, however, there is still a fast capacity fading during the subsequent 15-80 cycles. A reversible charge capacity of 462.7 mAh g^{-1} is retained after 80 cycles. Compared with Fe_2O_3/GAs, Fe-Fe_3O_4@C/GAs shows very stable cycling performances throughout 80 cycles. There is almost no capacity fading for the composite and a capacity of ~600 mAh g^{-1} can be still retained after 80 cycles. This should be largely ascribed to the presence of carbon-coating structure[46], which is used to increase the mechanical stability and electrical conductivity of Fe_3O_4 particles.

Besides the similar beneficial effect to the carbon coating suggested above, the 3D interconnected GAs substrate can also facilitate the electrolyte infiltration and the diffusion of ions and charge. Fig. 6e shows the cycling performances of FeS_2@C/S-GAs and FeS_2 at 0.1 C. Compared with the retained capacity (280.7 mAh g^{-1}) of pristine FeS_2, FeS_2@C/S-GAs has a substantially larger reversible capacity (~1000 mAh g^{-1}) after 80 cycles. This large reversible capacity is also better than the Fe/Fe_3O_4@C/GAs electrode with a stable capacity of ~600 mAh g^{-1}. This good cycling stability should be ascribed to the beneficial effect of GAs support and carbon coating, which is similar to the stable Fe/Fe_3O_4@C/GAs electrode. The effect of S-doping has also been suggested to increase the lithium-storage active sites due to more defects generated in GAs as well as the electronic conductivity[40,44,47]. SEM and TEM images of the FeS_2@C/S-GAs electrode after 80 cycles are presented in Fig. S7, Supporting Information. Due to the presence of carbon black and the PVDF binder, the carbon coating nanocluster structure cannot be identified. However, the three-dimensional GAs structure can be roughly observed (SEM image) and it is indicated that there are no large agglomerated particles during cycling (TEM image).

Fig. 6f shows rate capabilities of FeS_2@C/S-GAs and pristine FeS_2 at different current densities. When the current density increases from 0.1 C to 1 C, 2 C, 5 C, the reversible capacities of FeS_2@C/S-GAs change from ~1000 mAh g^{-1} to 705 mAh g^{-1}, 634 mAh g^{-1}, 455 mAh g^{-1}, respectively, which are substantially larger than the observed reversible capacities for pristine FeS_2 (from ~800 mAh g^{-1} to ~300 mAh g^{-1},

125 mAh g^{-1}, 75 mAh g^{-1}, respectively at the corresponding current densities). The good rate capability of the FeS_2@C/S-GAs electrode should be attributed to the shorter diffusion pathway, facilitated electrolyte infiltration and the increased electrical conductivity offered by the carbon coating and 3D interconnected GAs in the composite.[38] It is worthy noting that when the current density is changed back to 0.1 C, the reversible capacity of FeS_2@C/S-GAs can be returned to ~1000 mAh g^{-1}, but the value of pristine FeS_2 is only ~600 mAh g^{-1}. Fig. 7 shows the Nyquist plots of FeS_2@C/S-GAs and pristine FeS_2 after the 3th cycle. Compared with pristine FeS_2, FeS_2@C/S-GAs has a much smaller semicircle, indicating a lower charge transfer resistance (R_{ct}) at the electrode interface.[20] Based on the equivalent circuit as shown in the inset of Fig. 7,[8] the R_{ct} of FeS_2@C/S-GAs is calculated to be 94.5 Ω, which is smaller than that of pristine FeS_2 (525.2 Ω).

Conclusions

In summary, a series of Fe-based electrodes including Fe_2O_3/GAs, Fe-Fe_3O_4@C/GAs and FeS_2@C/S-GAs composites have been successfully synthesized in this work. GAs supported Fe_2O_3 nanocluster was first prepared by a solvothermal method and then converted to carbon coated Fe-Fe_3O_4 in a chemical vapor deposition process. The final product of FeS_2@C/S-GAs was obtained by a subsequent thermal sulfuration treatment. The FeS_2@C/S-GAs electrode is found to be more suitable as the electrode for lithium ion batteries compared to Fe_2O_3/GAs and Fe-Fe_3O_4@C/GAs electrodes. It delivers a large reversible capacity of ~1000 mAh g^{-1} at 0.1 C with a

good rate capability (reversible capacities of ~700, 630, and 450 mAh g^{-1} observed at 1, 2, and 5 C respectively). These good electrochemical performances have been mainly attributed to the synergetic effect of carbon coating, GAs support, and sulfur doping.

Acknowledgments

The authors gratefully acknowledge the follow-up Program for Professor of Special Appointment in Shanghai (Eastern Scholar), the National Natural Science Foundation of China (51271105), and Innovative Research Team (IRT13078) for financial support. The authors also thank Lab for Microstructure, Instrumental Analysis and Research Center, Shanghai University, for materials characterizations.

References

1 N. A. Kaskhedikar and J. Maier, *Adv. Mater.*, 2009, **21**, 2664.

2 M. G. Kim and J. cho, *Adv. Funct. Mater.*, 2009, **19**, 1497.

3 A. Manthiram, *J. Phys. Chem. Lett.*, 2011, **2**, 176.

4 F. Y. Cheng, J. Liang, Z. L. Tao and J. Chen, *Adv. Mater.*, 2011, **23**, 1695.

5 Z. Y. Zhou, N. Tian, J. T. Li, I. Broadwell and S. G. Sun, *Chem. Soc. Rev.*, 2011, **40**, 4167.

6 G. X. Gao, S. Y. Lu, B. T. Dong, Z. C. Zhang, Y. S. Zheng and S. J. Ding, *J. Mater. Chem. A*, 2015, **3**, 4716.

7 S. H. Zhao, D. Xie, X. D. Yu, Q. M. Su, J. Zhang, G. H. Du, *Mater. Lett.*, 2015, **142**, 287.

8 J. Kan and Y. Wang, *Sci. Rep.*, 2013, **3**, 3502.

9 L. Q. Lu and Y. Wang, *J. Mater. Chem.*, 2011, **21**, 17916.

10 Y. Q. Zou and Y. Wang, *Nanoscale*, 2011, **3**, 2615.

11 C. Xu, Y. Zeng, X. H. Rui, N. Xiao, J. X. Zhu, W. Y. Zheng, J. Chen, W. L. Liu, H. T. Tan, H. H. Hng and Q. Y. Yan, *ACS Nano*, 2012, **6**, 4713.

12 B. Wu, H. H. Song, J. S. Zhou and X. H. Chen, *Chem. Commun.*, 2011, **47**, 8653.

13 L. S. Li, M. C. Acevedo, S. N. Girard and S. Jin, *Nanoscale*, 2014, **6**, 2112.

14 D. Zhang, Y. J. Mai, J. Y. Xiang, X. H. Xia, Y. Q. Qiao and J. P. Tu, *J. Power Sources*, 2012, **217**, 229.

15 Z. Q. Wang, X. Li, Y. Yang, Y. J. Cui, H. G. Pan, Z. Y. Wang, B. L. Chen and G. D. Qian, *J. Mater. Chem. A*, 2014, **2**, 7912.

16 Y. Gu, Y. Xu and Y. Wang, *ACS Appl. Mater. Interfaces*, 2013, **5**, 801.

17 L. Mei, C. Xu, T. Yang, J. M. Ma, L. B. Chen, Q. H. Li and T. H. Wang, *J. Mater. Chem. A*, 2013, **1**, 8658.

18 T. Evans, D. M. Piper, S. C. Kim, S. S. Han, V. Bhat, K. H. Oh and S. H. Lee, *Adv. Mater.*, 2014, **26**, 7386.

19 L. Fei, Y. F. Jiang, Y. Xu, G. Chen, Y. L. Li, X. Xu, S. G. Deng and H. M. Luo, *J. Power Sources*, 2014, **265**, 1.

20 L. Fei, Q. L. Lin, B. Yuan, G. Chen, P. Xie, Y. L. Li, Y. Xu, S. G. Deng, S. Smirnov and H. M. Luo, *ACS Appl. Mater. Interfaces*, 2013, **5**, 5330.

21 J. Y. Luo, H. D. Jang, T. Sun, L. Xiao, Z. He, A. P. Katsoulidis, M. G. Kanatzidis, J. M. Gibson and J. X. Huang, *ACS Nano*, 2011, **5**, 8943.

22 J. Y. Luo, H. D. Jang and J. X. Huang, *ACS Nano*, 2013, **7**, 1464.

23 W. W. Sun and Y. Wang, *Nanoscale*, 2014, **6**, 11528.

24 Y. Gu and Y. Wang, *RSC Adv.*, 2014, **4**, 8582.

25 L. Y. Liang, Y. M. Xu, Y. Lei and H. M. Liu, *Nanoscale*, 2014, **6**, 3536.

26 C. H. Tan, J. Cao, A. M. Khattak, F. P. Cai, B. Jiang, G. Yang and S. Q. Hu, *J. Power Sources*, 2014, **270**, 28.

27 R. H. Wang, C. H. Xu, J. Sun and L. Gao, *Sci. Rep.*, 2014, **4**, 7171.

28 Z. S. Wu, S. B. Yang, Y. Sun, K. Parvez, X. L. Feng and K. Müllen, *J. Am. Chem. Soc.*, 2012, **134**, 9082.

29 Y. Hou, B. Zhang, Z. H. Wen, S. M. Cui, X. R. Guo, Z. He and J. H. Chen, *J. Mater. Chem. A*, 2014, **2**, 13795.

30 M. X. Chen, C. C. Zhang, X. C. Li, L. Zhang, Y. L. Ma, L. Zhang, X. Y. Xu, F. L. Xia, W. Wang and J. P. Gao, *J. Mater. Chem. A*, 2013, **1**, 2869.

31 H. K. Youn, J. Kim and W. S. Ahn, *Mater. Lett.*, 2011, **65**, 3055.

32 Y. Gu, F. D. Wu and Y. Wang, *Adv. Funct. Mater.*, 2013, **23**, 893.

33 T. Bhardwaj, A. Antic, B. Pavan, V. Barone and B. D. Fahlman, *J. Am. Chem. Soc.*, 2010, **132**, 12556.

34 J. P. Paraknowitsch and A. Thomas, *Energy Environ. Sci.*, 2013, **6**, 2839.

35 A. L. M. Reddy, A. Srivastava, S. R. Gowda, H. Gullapalli, M. Dubey and P. M. Ajayan, *ACS Nano*, 2010, **4**, 6337.

36 L. Q. Lu and Y. Wang, *Electrochem. Commun.*, 2012, **14**, 82.

37 S. Q. Chen and Y. Wang, *J. Mater. Chem.*, 2010, **20**, 9735.

38 L. Xiao, D. Q. Wu, S. Han, Y. S. Huang, S. Li, M. Z. He, F. Zhang and X. L. Feng, *ACS Appl. Mater. Interfaces*, 2013, **5**, 3764.

39 Y. Ma, G. Ji and J. Y. Lee, *J. Mater. Chem.*, 2011, **21**, 13009.

40 Y. S. Yun, V. D. Le, H. Kim, S. J. Chang, S. J. Baek, S. J. Park, B. H. Kim, Y. H. Kim, K. Kang and H. J. Jin, *J. Power Sources*, 2014, **262**, 79.

41 H. L. Poh, P. Simek, Z. Sofer and M. Pumera, *ACS Nano*, 2013, **7**, 5262.

42 J. Xia, J. Q. Jiao, B. L. Dai, W. D. Qiu, S. X. He, W. T. Qiu, P. K. Shen and L. P. Chen, *RSC Advances*, 2013, **3**, 6132.

43 G. M. Zhou, D. W. Wang, F. Li, P. X. Hou, L. C. Yin, C. Liu, G. Q. Lu, I. R. Gentle and H. M. Cheng, *Energy Environ. Sci.*, 2012, **5**, 8901.

44 W. Ai, Z. M. Luo, J. Jiang, J. H. Zhu, Z. Z. Du, Z. X. Fan, L. H. Xie, H. Zhang, W. Huang and T. Yu, *Adv. Mater.*, 2014, **26**, 6186.

45 W. L. Liu, X. H. Rui, H. T. Tan, C. Xu, Q. Y. Yan and H. H. Hng, *RSC Adv.*, 2014, **4**, 48770.

46 W. Fan, W. Gao, C. Zhang, W. W. Tjiu, J. S. Pan and T. X. Liu, *J Mater. Chem.*, 2012, **22**, 25108.

47 Y. Yan, Y. X. Yin, S. Xin, Y. G. Guo and L. J. Wan, *Chem. Commun.*, 2012, **48**, 10663.

Figure Captions

Scheme. 1 Schematic illustration showing the stepwise preparation process of Fe_2O_3/GAs, Fe-Fe_3O_4@C/GAs, and FeS_2@C/S-GAs.

Fig. 1 (a) XRD patterns of Fe_2O_3/GAs, Fe-Fe_3O_4@C/GAs and FeS_2@C/S-GAs. (b) TGA curve of FeS_2@C/S-GAs and GAs, (c) Raman spectrum of GAs, Fe-Fe_3O_4@C/GAs and FeS_2@C/S-GAs. Nitrogen sorption isotherms of (d) GAs, (e) Fe-Fe_3O_4@C/GAs and (f) FeS_2@C/S-GAs.

Fig. 2 The digital photographs of Fe_2O_3/GAs: (a) before freeze-drying and (b) after freeze-drying. The obtained Fe_2O_3/GAs product: (c-d) SEM images and (e, f) TEM images.

Fig. 3 The obtained Fe-Fe_3O_4@C/GAs product: (a, b) SEM images and (c, d) TEM images.

Fig. 4 The obtained FeS_2@C/S-GAs product: (a, b, c) SEM images, (d) the EDS spectrum and (e, f) TEM images. The inset image of (f) showing the carbon layer.

Fig. 5 XPS spectra of FeS_2@C/S-GAs: (a) the survey spectrum, (b) C 1s, (c) Fe 2p and (d) S 2p.

Fig. 6 Cyclic voltammograms of (a) pristine FeS_2 and (b) FeS_2@C/S-GAs at a scan rate of 0.1 mV s^{-1}. (c) The first and second cycle discharge (lithium insertion) and charge (lithium extraction) curves of FeS_2@C/S-GAs and pristine FeS_2 at 0.1 C. (d) Cycling performances of GAs, Fe_2O_3/GAs, Fe_2O_3 and Fe-Fe_3O_4@C/GAs at 0.1 C. Cycling performances of FeS_2@C/S-GAs and FeS_2: (e) 0.1 C and (f) rate capability.

Fig. 7 Nyquist plots of pristine FeS_2 and FeS_2@C/S-GAs electrodes.

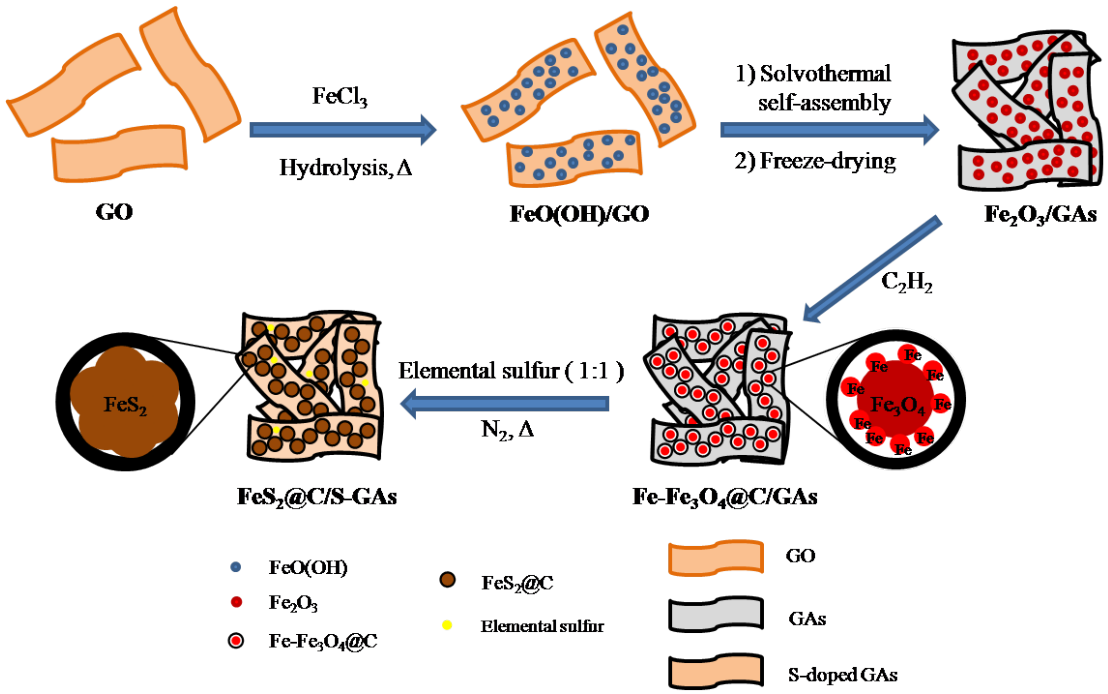

Scheme. 1 Schematic illustration showing the stepwise preparation process of Fe_2O_3/GAs, Fe-Fe_3O_4@C/GAs, and FeS_2@C/S-GAs.

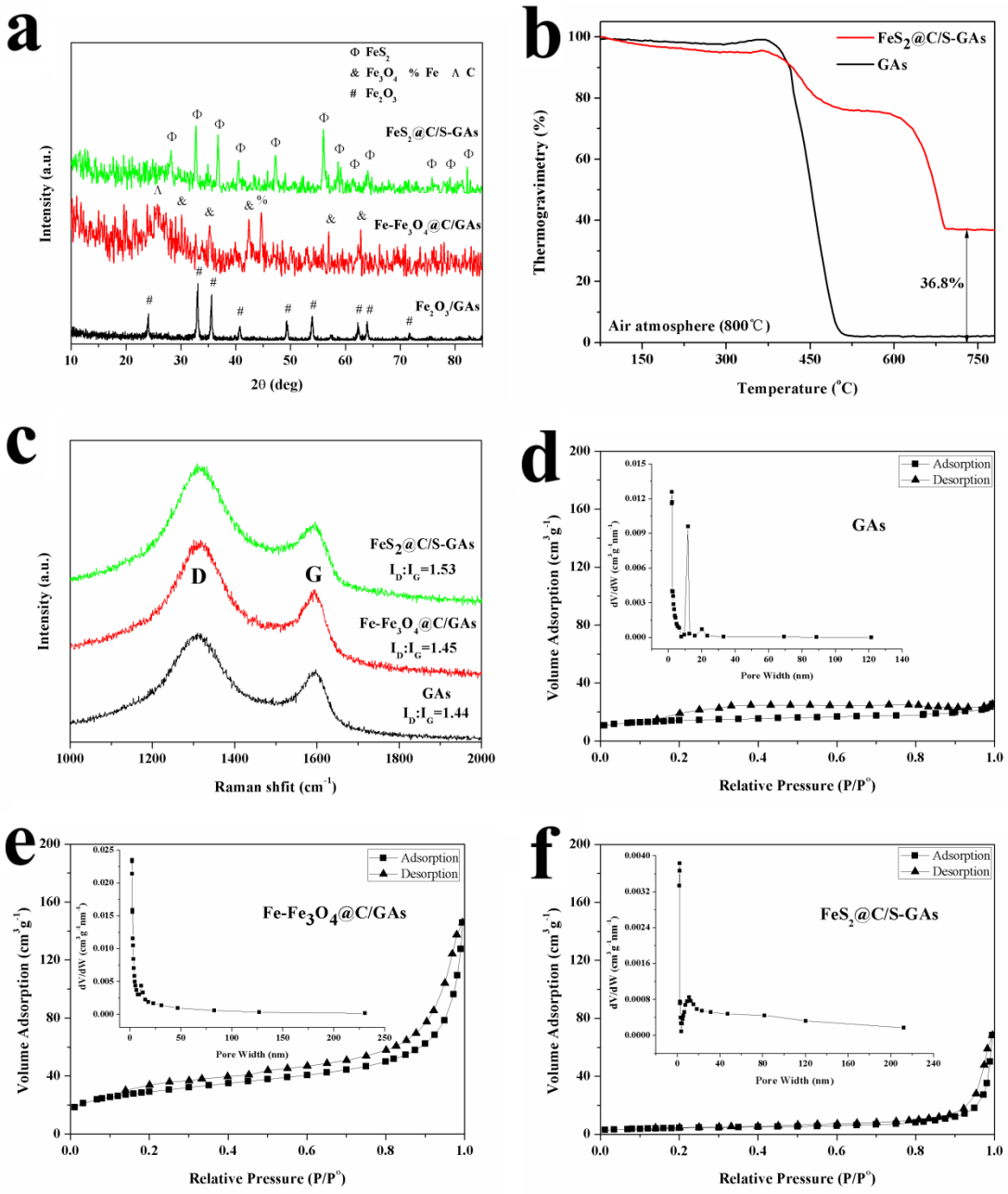

Fig. 1 (a) XRD patterns of Fe_2O_3/GAs, Fe-Fe_3O_4@C/GAs and FeS_2@C/S-GAs. (b) TGA curve of FeS_2@C/S-GAs and GAs, (c) Raman spectrum of GAs, Fe-Fe_3O_4@C/GAs and FeS_2@C/S-GAs. Nitrogen sorption isotherms of (d) GAs, (e) Fe-Fe_3O_4@C/GAs and (f) FeS_2@C/S-GAs.

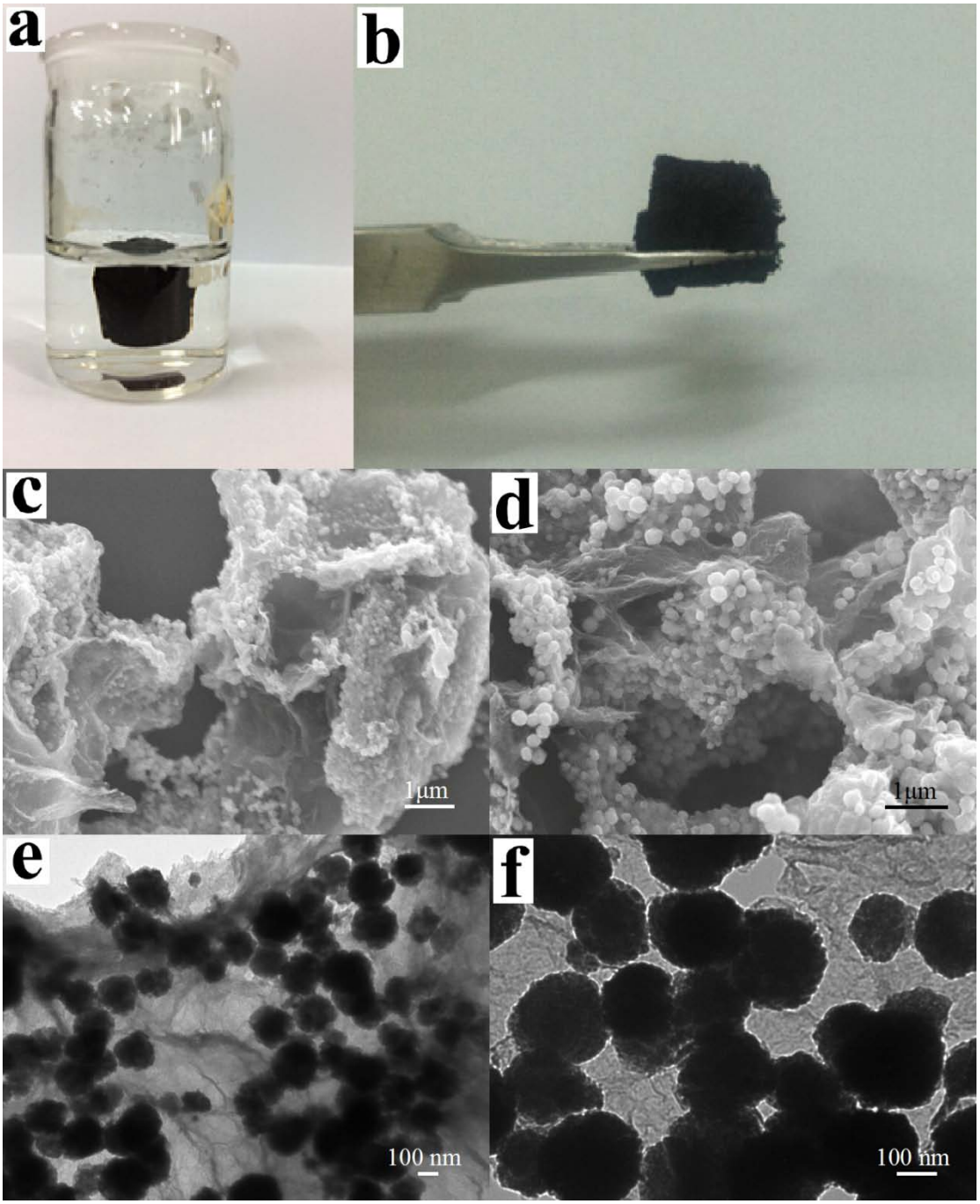

Fig. 2 The digital photographs of Fe_2O_3/GAs: (a) before freeze-drying and (b) after freeze-drying. The obtained Fe_2O_3/GAs product: (c-d) SEM images and (e, f) TEM images.

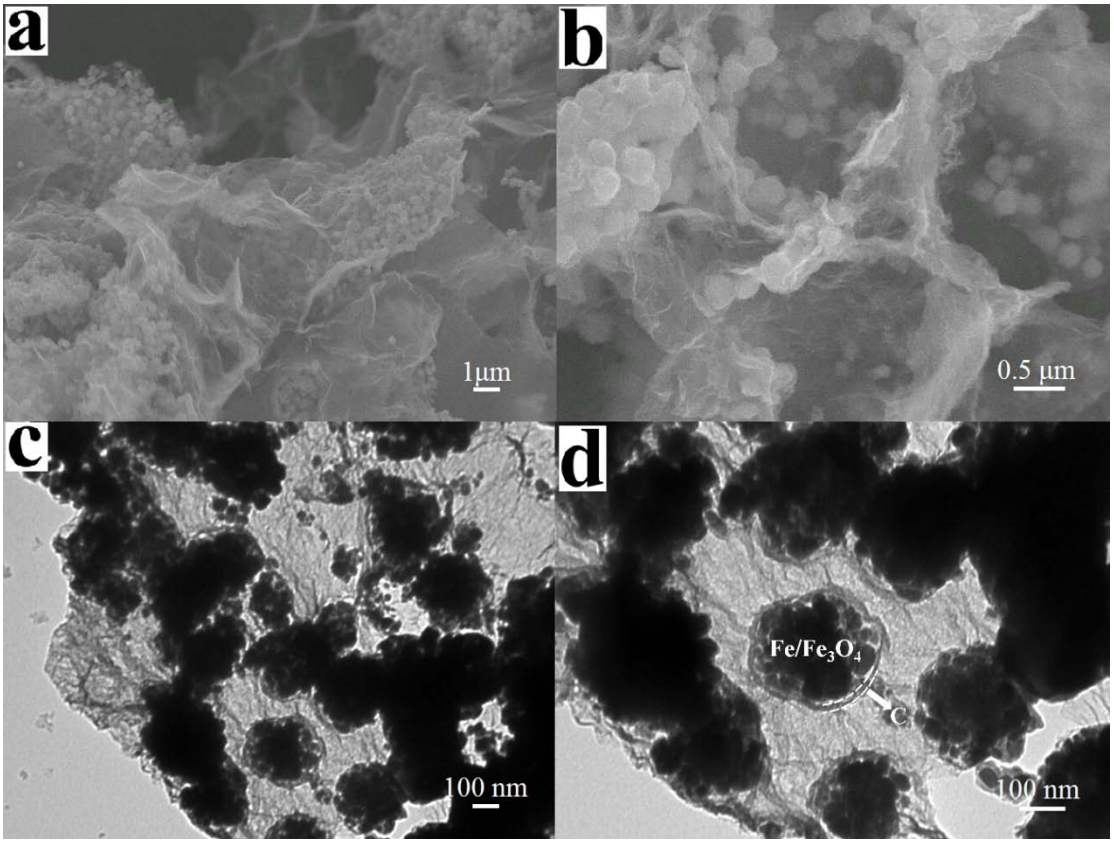

Fig. 3 The obtained Fe-Fe_3O_4@C/GAs product: (a, b) SEM images and (c, d) TEM images.

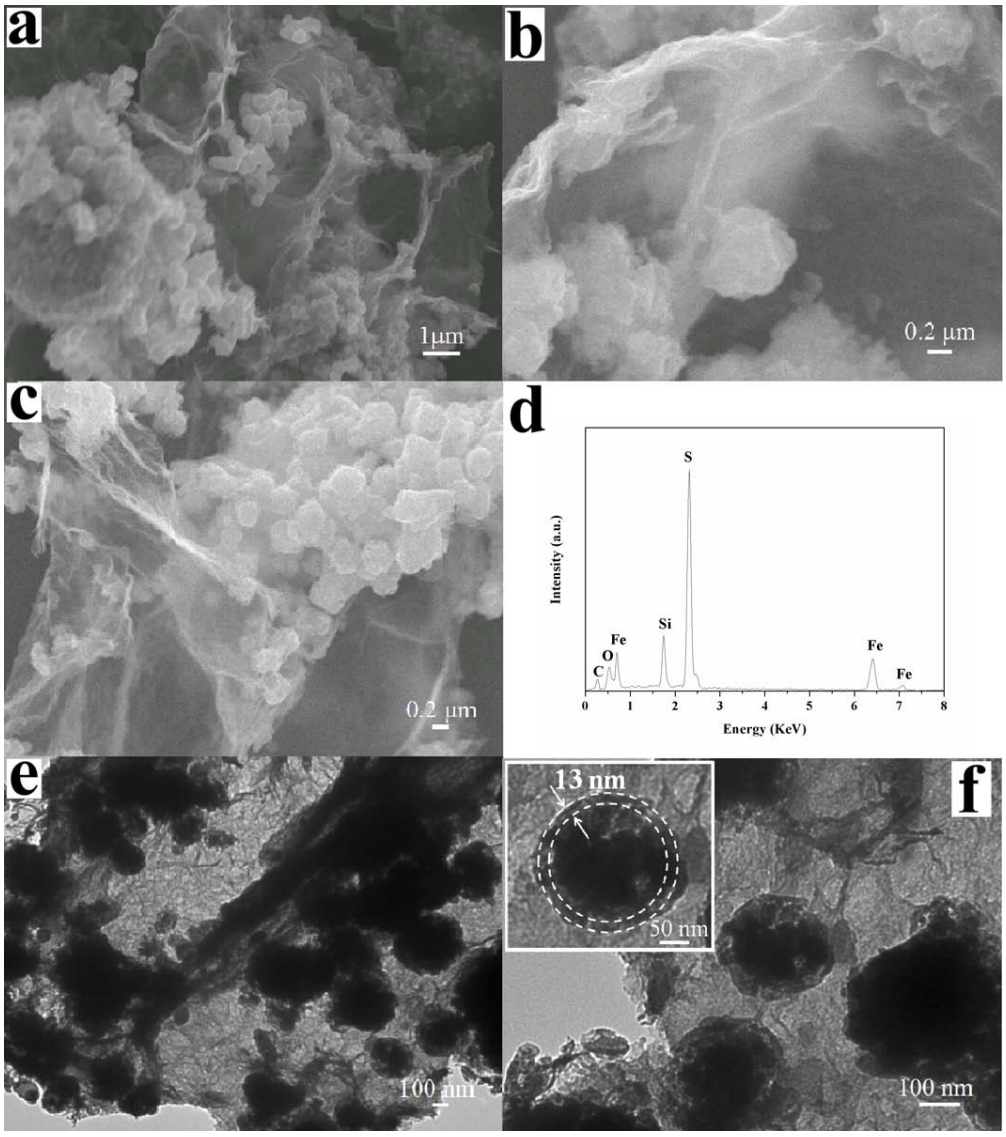

Fig. 4 The obtained FeS_2@C/S-GAs product: (a, b, c) SEM images, (d) the EDS spectrum and (e, f) TEM images. The inset image of (f) showing the carbon layer.

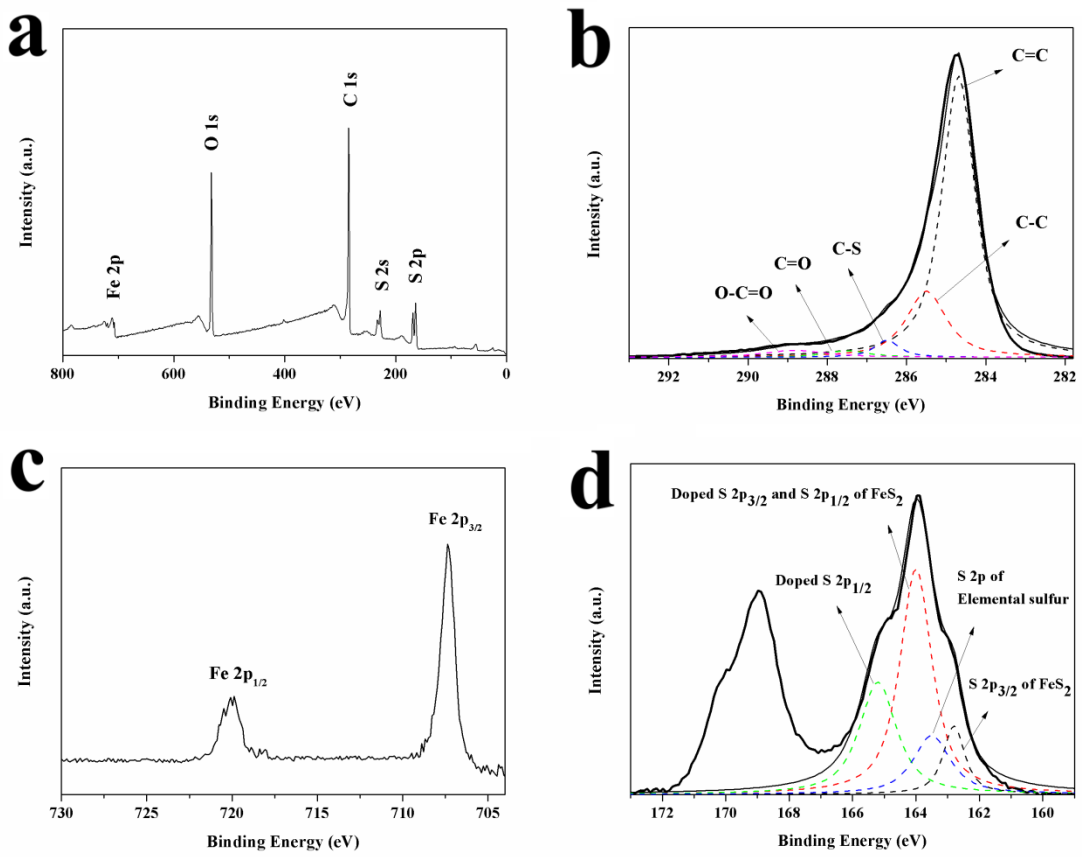

Fig. 5 XPS spectra of FeS_2@C/S-GAs: (a) the survey spectrum,(b) C 1s, (c) Fe 2p and (d) S 2p.

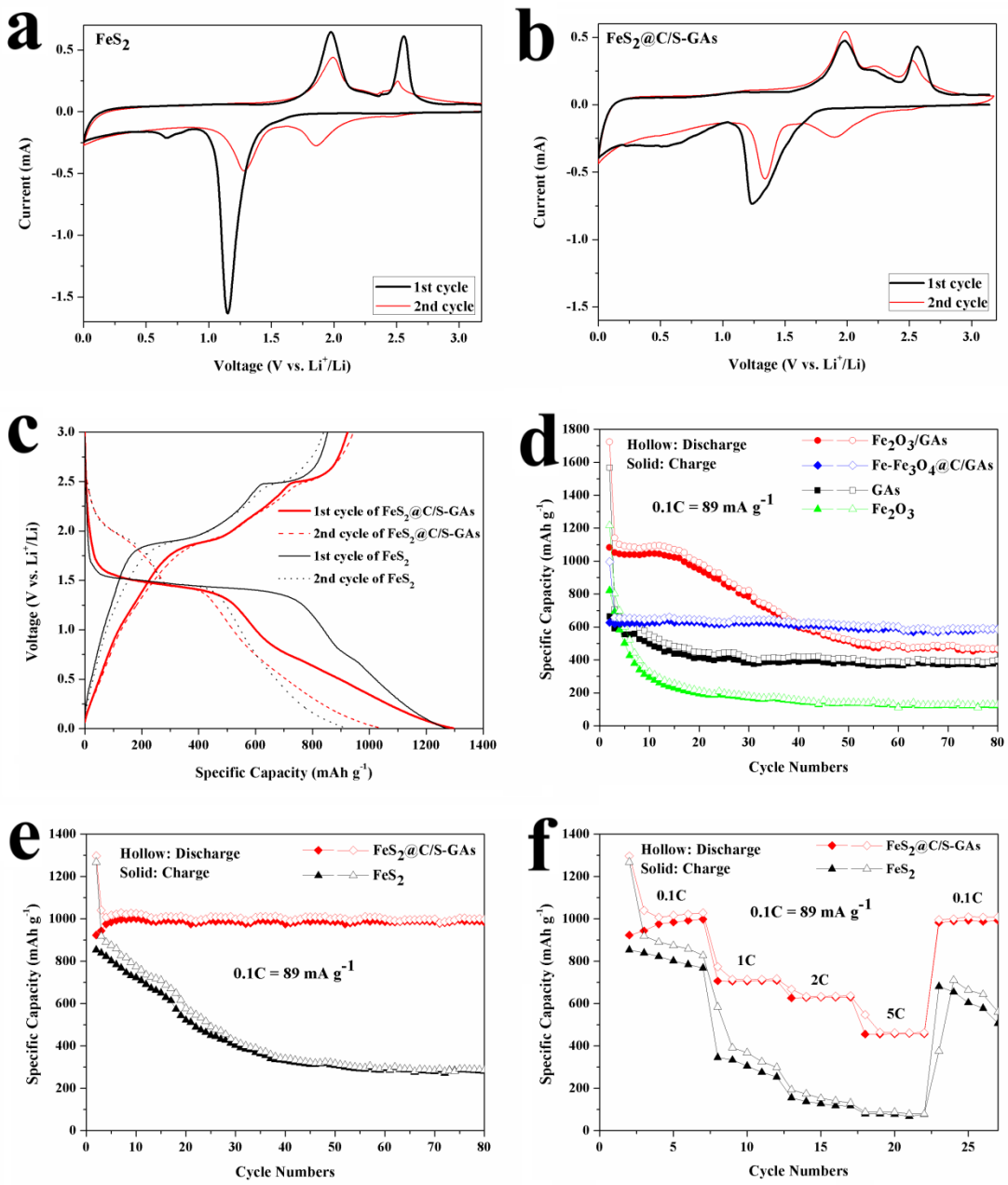

Fig. 6 Cyclic voltammograms of (a) pristine FeS_2 and (b) FeS_2@C/S-GAs at a scan rate of 0.1 mV s^{-1}. (c) The first and second cycle discharge (lithium insertion) and charge (lithium extraction) curves of FeS_2@C/S-GAs and pristine FeS_2 at 0.1 C. (d) Cycling performances of GAs, Fe_2O_3/GAs, Fe_2O_3 and Fe-Fe_3O_4@C/GAs at 0.1 C. Cycling performances of FeS_2@C/S-GAs and FeS_2: (e) 0.1 C and (f) rate capability.

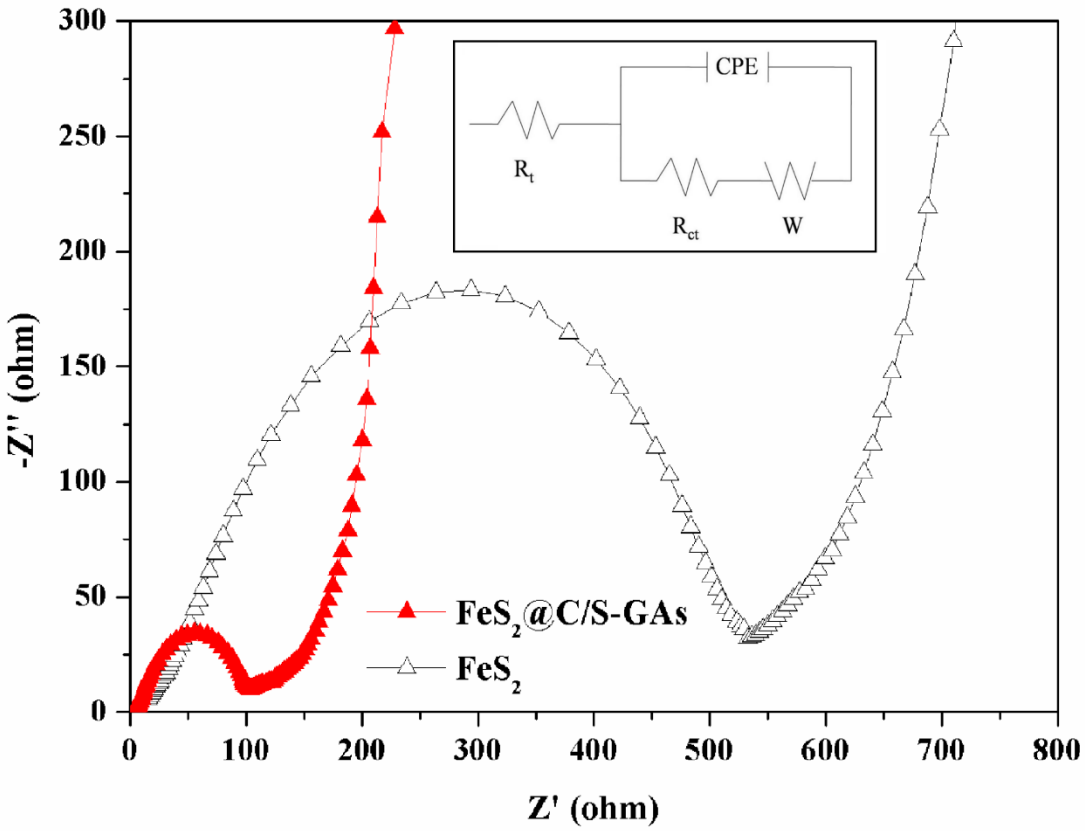

Fig. 7 Nyquist plots of pristine FeS_2 and FeS_2@C/S-GAs electrodes.

Graphical abstract

Graphene aerogels supported Fe_2O_3, Fe-Fe_3O_4@C, and FeS_2@C composites are prepared in a stepwise topotactical conversion process and exhibit good lithium ion storage properties.

Topotactical Conversion of Carbon Coated Fe-based Electrodes on Graphene Aerogels for Lithium Ion Storage

Feiying Jing and Yong Wang*

Keywords: graphene aerogels, carbon coating, sulfur doping, iron sulfide, iron oxide